THE JOURNAL OF PHYSICAL CHEMISTRY B
A JOURNAL OF THE AMERICAN CHEMICAL SOCIETY

Open Access
This article is licensed under CC-BY-NC-ND 4.0

pubs.acs.org/JPCB
Article

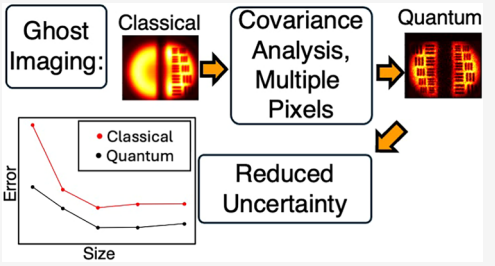
Comparison of the Error Incurred in the Measurement of Nonblinking, Nonpoint-Source Objects Using Classical and Quantum Imaging

Dorian F. Twedt-Gutierrez, Emily A. Smith, Jacob W. Petrich,* and Xueyu Song*

Cite This: J. Phys. Chem. B 2026, 130, 10826−10835
Read Online

ACCESS | Metrics & More | Article Recommendations | Supporting Information

ABSTRACT: We present another step in our efforts to expand far-field imaging beyond the diffraction limit and beyond the limitations imposed by fluorescent labels. The model system we examine is based on the exploitation of entangled photon pairs at 810 nm generated by spontaneous parametric down conversion (SPDC) of a 405 nm source to resolve the separations of the line pairs of a series of two-dimensional objects. A ghost-imaging optical system directs signal and idler photons along two paths, one of which contains the objects. Images are constructed using a covariance analysis of the entangled pairs using typically 10^6 frames collected with an EMCCD detector that was calibrated to account for the number of entangled pairs of photons, which is necessary for an accurate determination of the resolution and its comparison with the classical method. Conservation of momentum requires that there is inversion symmetry between the transverse **k** vectors of the photons passing through the target and their entangled counterparts directed along the targetless path. Our covariance analysis not only addresses this symmetry but also that the width of the covariance peak is broader than a single pixel owing to the nature of SPDC and the details of the optical arrangement. Consideration of this broadening provides significant improvement of the image quality. The Heisenberg limit (HL) is achieved within experimental error: using the same optical alignment, the resolution obtained with entangled pairs of 810 nm photons is, within experimental error, twice that obtained with classical 810 nm photons. More importantly, the error bars of measurements with 810 nm entangled pairs are quantified by the Cramér-Rao lower bound (CRLB) and compared with those of the classical measurements. While other workers have done quantum imaging on nonpoint sources, to our knowledge we are the first group that not only has done the quantum imaging ***but also*** has compared the CRLB ***and*** the measured error of the quantum and classical measurements for a series of different-sized objects. (Similar comparisons have, however, been made for systems that can be approximated as point sources, e.g., determining the separation of two laser beams).



INTRODUCTION

We present another step in our efforts[1,2] to provide an alternative to the use of "blinking" fluorescent systems[3] to defeat the diffraction limit and to achieve a method of super-resolution imaging that can eventually be extended to individual molecules. Obtaining super-resolution with a Raman source is particularly appealing because Raman spectroscopy provides direct information on the chemical nature of the system through its vibrational modes. Thus, our first attempt[1,4] explored the possibility of using a saturated coherent anti-Stokes Raman scattering (CARS) signal that was demodulated at higher frequencies of the pump modulation frequency, *f*. This experiment depends on the saturation of the vibrational transition. The more intense center of a Gaussian laser-beam profile provides more saturation than the wings. Hence, detection of higher modulation frequencies affords more spatial resolution than lower modulation frequencies. At the third harmonic, 3*f*, theory predicted an improvement of spatial resolution by a factor of 1.7 for nanodiamond particles. Experiments confirmed that spatial resolution was enhanced by a factor of 2. Unfortunately, the applicability of saturated CARS is limited to robust samples such as diamond; and even for diamond, extraction of harmonics beyond 3*f* was not feasible because the pump intensities required for sufficient saturation induce sample damage.

Another avenue was investigated. In conventional imaging methods often referred to as classical or "direct" because they rely upon the direct detection of single photons from individual emitters, each emitter is approximated as a point source that is broadened by the response of the detection system to produce its point-spread function (PSF). The PSF determines the resolution of an imaging system. If one computes the image of two emitters (with a reasonable form

Received: May 19, 2026
Revised: September 14, 2026
Accepted: September 17, 2026
Published: September 30, 2026



ACS Publications
© 2026 The Authors. Published by American Chemical Society

https://doi.org/10.1021/acs.jpcb.6c03297
J. Phys. Chem. B 2026, 130, 10826−10835

Downloaded from pubs.acs.org/jpcbfk/article-pdf/130/41/10826/6872096/acs.jpcb.6c03297.pdf by IOWA STATE UNIV user on 15 October 2026

for the PSF, such as a Gaussian function) as the separation between them decreases, it is straightforward to find that the error in the measurement diverges (this divergence for separated point emitters is called "Rayleigh's curse"). The alternate strategy was inspired by Tsang et al.[5] by appreciating that a more systematic and useful means of characterizing the error in the measurement of, for example, the separation between two point-sources is to use the Fisher information (FI) matrix, obtained by treating the problem as one of parameter estimation.[6,7] (The inverse of the FI is the Cramér-Rao lower bound, which is equal to the variance of the measurement). Tsang et al.[5] demonstrated that the quantum Fisher information (qCRLB)[6] suggests avenues of defeating "Rayleigh's curse". Not only does it not diverge with decreasing separation between emitters, *it saturates at a finite value*. Thus, our next attempt by Santra et al.[2] specifically used the CRLB to study how the measurements of centroids *and* separations of objects using the detection of the interference of single-photon amplitudes can be improved by exploiting the interference of spatial modes. (Interference of one-photon amplitudes is to be contrasted with that of two-photon amplitudes, discussed extensively in Shih's text[8]). This work[2] employed optical heterodyning, which is essentially an interference technique. For example, if a Gaussian point-spread function (a TEM_{00} mode) of a point-emitter is displaced with respect to the origin of the optical system, photons in the higher-order transmission electron microscopy (TEM) modes carry information about that displacement. Information concerning the displacement can be extracted from photons in these higher-order modes. These photons can be collected by optical heterodyning, which exploits the large gain in a detector's response to an optical signal from an emitter coupled to a local oscillator, which is prepared in the TEM of interest, e.g., TEM_{10}. We generalized and developed the heterodyning technique to localize point-emitters via the detection of higher-order spatial modes. We also developed a theoretical approach to find a practical estimation limit of the localization parameters using a realistic model for noise. To demonstrate the applicability of the method, we designed experiments where a laser is a surrogate for one and two point-emitters. Using the Fisher information (FI) and its accompanying Cramér-Rao lower bound (CRLB), we demonstrated super-resolution localization: objects can be localized to roughly 2 to 3 orders of magnitude of their PSF's size for a given optical system.

In this paper, we continue our efforts to broaden the scope of super-resolution measurements beyond the limits of fluorescence-based techniques. We explore the role of entangled, spontaneous parametric down-converted (SPDC) photons in resolving not a point source, but a target with a particular shape, at the Heisenberg limit (HL). And we make a quantitative comparison of the reduction in the standard deviations of measurements in going from a classical, unentangled source to a quantum, entangled source. Specifically, we demonstrate the slowing down of the divergence of the CRLB for distance measurements of nonpoint sources. Several examples achieving the HL, or suggesting the possibility of enhanced resolution, have been presented. Defienne and co-workers[9,10] and Padgett and co-workers[11,12] have discussed many aspects of the details involved in the use of entangled photons for imaging. Unternährer et al.[13] image at the HL by detecting coincidences of the signal-idler pair in time. Unfortunately, their detector was limited to 32 × 32 pixels and thus was not practical for high-resolution imaging. Jachura and Chrapkiewicz[14,15] and Parniak et al.[16] exploit Hong-Ou-Mandel HOM interferometry of biphoton probability amplitudes to achieve enhanced resolution. In two papers, Devaux et al.[17,18] provide a detailed exploration of the potential for HOM interferometry to provide spatial resolution using EMCCD detectors with no capability for direct timing of coincident events. Finally, He et al.[19] have achieved the HL using only the spatial resolution provided by EMCCD detectors and a covariance analysis of signal-idler coincidences to attain the HL.

To our knowledge, however, ours is the first analysis of a target not approximated as a point source to demonstrate the reduced divergence of the error in distance measurements using quantum imaging. Namely, not only have we performed quantum imaging with a series of *nonpoint sources* but we have also compared the error in these quantum images with those from the corresponding classical images. And we have additionally compared the CRLBs of these quantum and classical images. In the process, we have generated a covariance procedure that allows the automatic generation of a quantum image without the need for precise mechanical alignment of the beam path and that accounts for the momentum-correlation width of the signal-idler pair being greater than the size of a single pixel. We extend the covariance analysis to include neighborhoods of pixels rather than just single-pixel pairs. These comparisons are made possible, in part, because the efficiency of our EMCCD is calibrated for the detection of classical as well as entangled photons.

EXPERIMENTAL METHODS

Apparatus for Ghost Imaging

The experimental apparatus, motivated by that used by He et al.,[19] is shown in Figure 1. A 405 nm continuous-wave laser operating at 10 mW was cleaned to TEM_{00} using a polarization-maintaining, single-mode optical fiber, with a beam radius of 1050 μm. The laser provides degenerate time- and momentum-entangled 810 nm photons via spontaneous

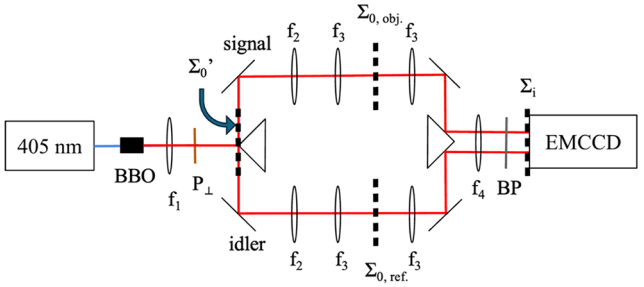


Figure 1. Schematic for ghost-imaging. A 405 nm laser illuminates a type-I β-barium borate crystal (BBO) to generate 810 nm SPDC photons. At a plane $\sum_0'$, the cone-shaped SPDC emission is split in half at a knife-edge right-angle prism mirror and directed along two symmetric paths. On one, an object of interest (1951 USAF resolution test chart) is introduced in the object plane $\sum_{0,\,obj}$. The other path contains a piece of glass of the same thickness as that of the test chart in the reference plane, $\sum_{0,\,ref}$, to ensure the equivalence of the two optical paths. The SPDC half-beams are reunited by a second right-angle prism mirror, detected by an EMCCD detector at $\sum_i$. $P_\perp$= polarizer (horizontal). BP = bandpass filter. Lenses: f_1 = 50 mm, f_2 = 175 mm, f_3 = 9 mm objective lens (LIO-20X, Newport), f_4 = 250 mm. Lenses are placed such that there is a 4f system between adjacent $\sum$ planes.

Downloaded from pubs.acs.org/jpcbfk/article-pdf/130/41/10826/6872096/acs.jpcb.6c03297.pdf by IOWA STATE UNIV user on 15 October 2026

https://doi.org/10.1021/acs.jpcb.6c03297
J. Phys. Chem. B 2026, 130, 10826−10835

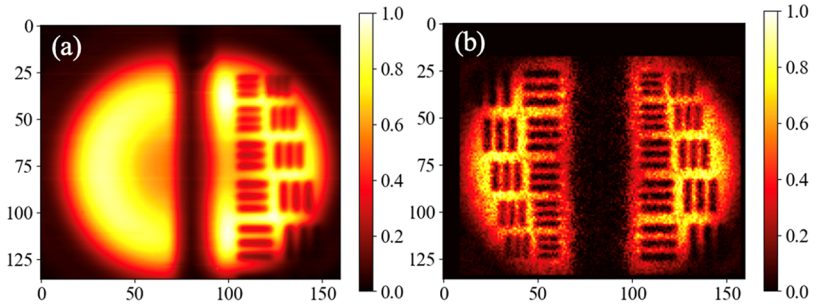


Figure 2. Classical image (a) is an accumulation of 1.5 million frames acquired using the apparatus in Figure 1. In each panel, the right half of the beam is from the object side of the ghost-imaging setup, where a USAF resolution test chart has been placed at $\sum_{0,obj}$. The quantum image (b) is generated from the covariance matrix with the same data set used to generate (a). The symmetric ghost images of the targets are on the left side of (b) and display the $\mathbf{k} = -\mathbf{k}$ symmetry.

parametric down-conversion (SPDC) from a type-I, β-barium borate crystal (BBO; NCBBO5300-405(I)-HA3, Newlight). A Glan-Thompson polarizer after the BBO crystal rejects residual 405 nm light. At the plane, $\sum_0'$, the cone-shaped SPDC emission is split in half at a knife-edge, right-angle, prism mirror (MRAK25-P01, Thorlabs) and sent to two symmetric paths. The cone shape is a result of the momentum conservation of the signal and idler photons generated by SPDC and is evidenced by the annulus shown in Figure 2. On one path, a positive 1951 USAF resolution test chart (58−198, Edmund Optics) is introduced in the object plane, $\sum_{0,obj}$. The other path is left undisturbed except for a piece of glass of the same thickness as the chart, which is placed in the reference plane $\sum_{0,ref}$ to maintain the symmetry of the two paths by ensuring that the photons traversing them have the same path length. The photons from the two paths are directed by a second right-angle prism mirror into an EMCCD camera (iXon Ultra 888, Andor) at $\sum_i$. An 810 nm bandpass filter (FBH810−10, Thorlabs) at the detector's input removes stray light and any remaining pump-beam light. Lenses are placed such that there is a 4f system between $\sum$ planes adjacent in series. For all data presented in this study, a 10 ms exposure time ("frame width") was used, and the photon flux at this power is sufficiently low to ensure photon-counting conditions, i.e., no more than one photon per pixel is detected per frame. After application of a threshold, classical images have a mean flux of 0.1045 ± 0.0005 photons/pixel. This is equivalent to 1000. ± 5 photons/frame, considering the dimensions of our frame. The detector was operated at −65 °C with an electron-multiplying gain of 1000. A vertical shift speed of 1.13 μs and a 10-MHz readout rate were used. 2 × 2 hardware binning is used for all data acquired. Data were processed using custom Fortran and Python scripts. Classical and quantum images are not smoothed or otherwise manipulated, aside from linear intensity scaling (e.g. normalization).

Counting Classical and Entangled Photons

Calibration of the EMCCD detector is required for an accurate determination of the number of photons, noise counts, and entangled pairs detected during an acquisition. Because of the stochastic nature of the electron-multiplying process, the raw signal provided by the detector, in counts, is proportional to the number of incident photons at a given threshold. The proportionality, however, at different thresholds is different. This threshold must be determined for a given experiment. The data in electron counts must be converted to bits, where 1 is representative of either a genuine incident photon or a noise count. A threshold condition must be applied

$$n_{e^-} \geq T \rightarrow 1(\text{"click"}); \qquad n_{e^-} < T \rightarrow 0 \tag{1}$$

n_{e^-} is the number of electron counts in the raw data for a given pixel and T is a chosen threshold. For our experiments, the intensity is sufficiently low that the probability of more than one photon incident upon the same pixel for one frame is negligible. The signal that is converted to 1 may be either a genuine photon detection, or a noise count

$$N_{click} = N_{true} + N_{noise} \tag{2}$$

A noise count may originate from intrinsic detector noise or from stray light. The calibration is performed using the SPDC beam itself in a manner described by Klyshko[20] and others.[21,22] The resulting function, $P_{NC}(T)$, represents the probability of a pixel reporting a noise count at a threshold T; and $\eta(T)$ is the quantum efficiency of an 810 nm photon at T. The procedure for obtaining $P_{NC}(T)$ and $\eta(T)$ are described in the Supporting Information. An important and useful aspect of this calibration method is that $\eta(T)$ is the quantum efficiency not only of the detector; it also includes optical losses incurred by the entire ghost-imaging optical system.[22]

In classical imaging, a photon-counting detector counts photons incident at each pixel. These photons are accumulated to build up an image. In the quantum-imaging case, however, the intensity of the image represents the covariance between pairs of pixels, which for SPDC are related by inversion symmetry. This covariance is proportional to the number of SPDC pairs used to generate the image. To compute the number of SPDC pairs, it is necessary to know the quantum efficiency of the detection of an 810 nm photon, η, as discussed in the previous paragraph.

For an entangled pair to contribute to a quantum image, however, *both* the signal and idler photons must be successfully detected. This is a process with probability η^2. In the event that either the signal or idler photon is scattered away by an obstruction in the beam path, or otherwise fails to be detected, the entangled photon pair has no contribution to the covariance intensity and the resulting quantum image. It is, therefore, equivalent to a noise count. Consequently, a given data set contains a much greater number of 810 nm photons than jointly detected SPDC pairs. As the quality of an image depends upon the number of photons used, an accurate comparison of classical and quantum images requires adjusting the number of frames so that the number of 810 nm photons used to generate a classical image matches the number of SPDC pairs for generating the quantum image.

Downloaded from pubs.acs.org/jpcbfk/article-pdf/130/41/10826/6872096/acs.jpcb.6c03297.pdf by IOWA STATE UNIV user on 15 October 2026

https://doi.org/10.1021/acs.jpcb.6c03297
J. Phys. Chem. B 2026, 130, 10826−10835

In classical imaging, after application of a threshold function, the signal collected from the EMCCD detector can come from either noise counts or, our case, 810 nm photons, which contribute to the classical image, eq 3 being the specific case of eq 2.

$$N_{\text{total}} = N_{810\text{ cts}} + N_{\text{noise cts}} \tag{3}$$

For any η, the number of individual 810 nm photons detected (on the object side) is related to the number of SPDC pairs emitted at the source by

$$N_{810\text{ cts}} = N_{\text{source pairs}}\eta \tag{4}$$

As the detection probability of a joint SPDC pair is η^2, the number of pairs detected is

$$N_{\text{pairs detected}} = N_{\text{source pairs}}\eta^2 \tag{5}$$

Substitution yields

$$N_{\text{pairs detected}} = N_{810\text{ cts}}\eta \tag{6}$$

As a result, for an accumulation of F frames that contains $N_{810\text{ cts}}$ 810 nm photons on the object side, approximately F/η frames are needed to generate a quantum image from $N_{810\text{ cts}}$ entangled pairs, ensuring that the number of 810 nm classical photons on the classical image matches the number of entangled pairs used to generate the quantum image.

Identifying the Covariance of Signal and Idler Photons for the Quantum Image

Fundamental to the construction of the quantum image is the identification of the covariance matrix of the signal and the idler photons as the joint probability of their coincidence and hence to equate this coincidence with the quantum image, QI. One half of the camera in Figure 1 registers, frame-by-frame, signal photons; the other half, idler photons. Because the exposure time of a frame is 10 ms, and thus incapable of identifying temporal coincidences, no conclusions can be made concerning the correlation with a photon on the signal half of the frame with its idler partner on the other half. Coincidences must be established by a frame-by-frame covariance computation. This computation starts with the appreciation that the covariance is imposed by the inversion symmetry of the wavevectors of the signal and the idler: $\mathbf{k} = -\mathbf{k}$. Starting with this, we can immediately write the following, where noise terms arising from nonentangled events, $\mathbf{k} \neq -\mathbf{k}$, tend to zero after a frame-by-frame average. (Events from nonentangled photons and from other noise can be assumed to be Poissonian and to average to zero, as they do not contribute to the covariance value.) The intensity value of the quantum image at a pixel, $\mathbf{k} = (i,j)$, can be given by

$$\text{cov}(I_{\mathbf{k}}, I_{-\mathbf{k}}) = \frac{1}{F}\sum_{n=1}^{F}(I_{(i,j);n} - \overline{I_{(i,j)}}(I_{(k,l);n} - \overline{I_{(k,l)}}) \tag{7}$$

In the above equation, the notation (i,j); n denotes the (i,j)-th pixel of the n-th frame (from F total frames); and I denotes the number of counts at that pixel. Note that $\mathbf{k}$, a vector, represents a pixel at a location (x,y), and k is an x-coordinate. The analysis of He et al.[19] presents the same conclusion: the covariance is the quantum image. It also, in practice, exploits the inversion symmetry of the wavevectors. But their reasoning differs. The mere detection of a signal photon on an isolated frame is not a coincidence given the exposure time of their detector. Nor can coincidence events be assumed to be Poissonian in order to justify setting a cross term to zero. A true coincidence for an entangled pair requires that the detection of an idler photon depends upon the detection of the signal photon and *vice versa*. They are a correlated pair. Without adequate time resolution, this coincidence must be established by the covariance.

Quantum-Image Algorithm

Owing to momentum conservation, the signal and idler photons of entangled pairs generated via SPDC are located by inversion symmetry about the center of the annulus of the SPDC distribution. The method of He et al.[19] to find the location of entangled photons requires an extremely precise determination of the location of the detected photons relative to each other. It also only allows coincidences detected at *one pair* of pixels to contribute the quantum image. Because, however, the joint-probability distribution of the position of an idler photon for a given signal photon (and *vice versa*) may be wider than a single pixel, QI algorithms that consider the data from only one pair of pixels can result in the neglect of coincidence events, diminishing the quality of the QI.

The $\overline{I_{i,j}}$ are obtained from every 25,000 frames for which the covariance is computed. Although roughly 10^6 frames are used to compute a quantum image, updating the average on a relatively short interval is needed to account for slight shifts in the target relative to the beam. As the joint probability distribution spans multiple pixels (Figure S2), we find the contrast-to-noise ratio of the quantum image is significantly improved by summing the covariance values between $\mathbf{k}$ and $-\mathbf{k}$, plus a neighborhood of L pixels around the central $-\mathbf{k}$ pixel, as depicted in Figure S3. Quantum images are thus constructed using

$$QI_{\mathbf{k}} = \frac{1}{2}\left[\sum_{m=1}^{L}\text{cov}(I_{\mathbf{k}}, I_{-\mathbf{k};m}) + \sum_{m=1}^{L}\text{cov}(I_{-\mathbf{k}}, I_{\mathbf{k};m})\right] \tag{8}$$

$I_{\mathbf{k};m}$ is the value of the pixel at position m around the central $\mathbf{k}$ pixel, as shown in Figure S2. For our experiments, $L = 9$ or $L = 21$ pixels are used. Although both of these directions, $\sum_{m=1}^{L}\text{cov}(I_{\mathbf{k}},I_{-\mathbf{k};m})$ and $\sum_{m=1}^{L}\text{cov}(I_{-\mathbf{k}},I_{\mathbf{k};m})$, should be equivalent after large F, slight variations due to differences in the performance of individual pixels and in optics and alignment are reduced by the averaging. (We assume that the only correlated signal present arises from biphotons; however, it is possible that other correlated phenomena contribute marginally to the covariance values, such as correlated noise and pixel cross-talk, which affects pixels in a neighborhood of a few pixels around one where a photon is incident). The matrix multiplication is performed via the corresponding OpenBLAS Fortran operation on a CPU and parallelized using OpenMP. Computation requires approximately 1 h per million frames on our desktop PC.

Finding the Center of Inversion Symmetry

Generating the quantum image from the covariance matrix at symmetric coordinates requires locating the center of inversion symmetry of the SPDC beam. With the two half-beams roughly centered in the detector acquisition window, the center of symmetry needs to be located within one pixel so that for each pixel at a position $\mathbf{k}$, the symmetric position $-\mathbf{k}$ can be determined. This requires a systematic method of finding the covariance peaks used to build the quantum image. The algorithm, described in the SI, allows automatic generation of a quantum image without the need for precise mechanical

Downloaded from pubs.acs.org/jpcbfk/article-pdf/130/41/10826/6872096/acs.jpcb.6c03297.pdf by IOWA STATE UNIV user on 15 October 2026

https://doi.org/10.1021/acs.jpcb.6c03297
J. Phys. Chem. B 2026, 130, 10826−10835

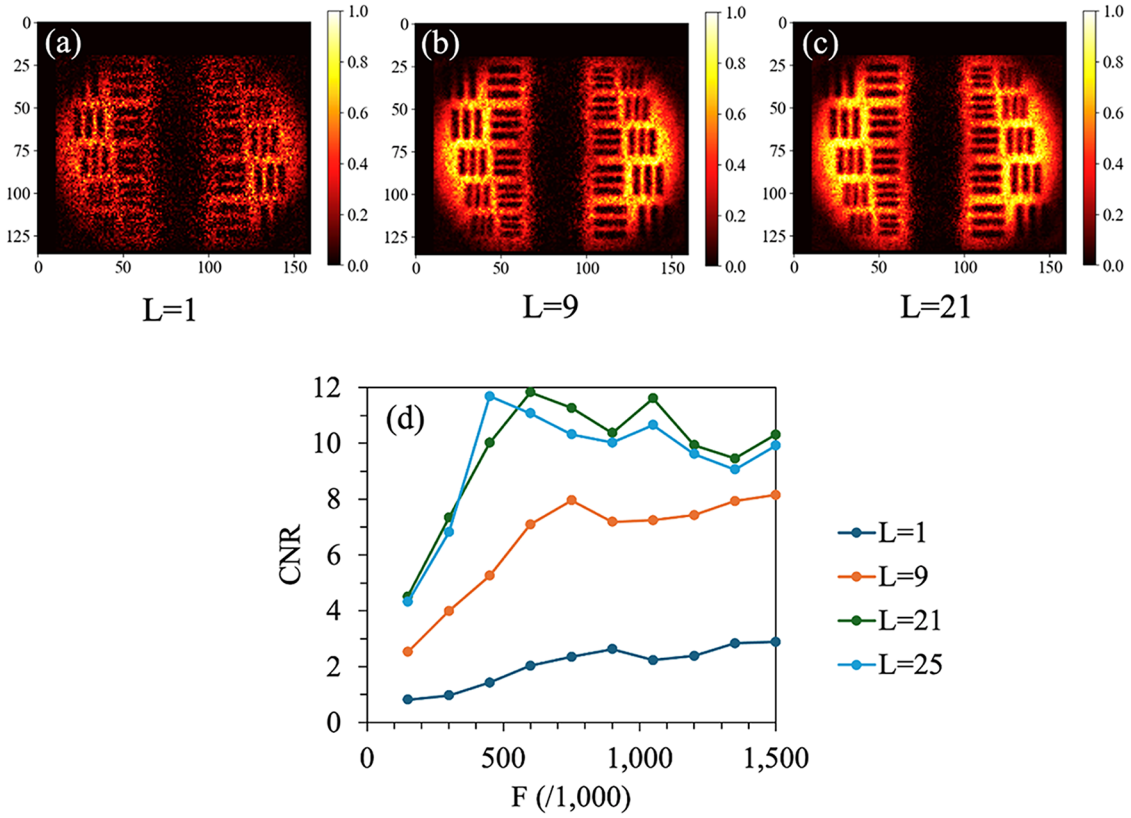


Figure 3. Varying integration limits to improve CNR. The integration limits of the covariance peak for each pixel are varied from $L = 1$ to $L = 25$, in a pattern shown in Figure S3, where $QI_{\mathbf{k}} = \frac{1}{2}[\sum_{m=1}^{L} \mathrm{cov}(I_{\mathbf{k}}, I_{-\mathbf{k};m}) + \sum_{m=1}^{L} \mathrm{cov}(I_{-\mathbf{k}}, I_{\mathbf{k};m})]$. Example images generated with the same data using $L = 1$, $L = 9$, and $L = 21$ are shown in panels (a)−(c). The CNR vs the number of frames, F, is plotted using various integration limits in panel (d). As the width of the $L = 21$ pattern is 5 pixels, and our MCW is 5.2 pixels, further increasing the integration limits beyond the MCW does not improve CNR. Integrating beyond $L = 1$, however, drastically improves the CNR.

alignment of the beam path. Nor does it require "manual" alignment of left and right panels in the software. It also corrects for shifting beam paths over the course of multiple acquisitions. Results of the procedure are given in Figures 2, 3, and 4.

Comparing Classical and Quantum Images

To provide a proper comparison with our methods and those of He et al.,[19] we follow them in evaluating the contrast-to-noise ratio, CNR, of our quantum images

$$\mathrm{CNR} = \frac{|\overline{I_1} - \overline{I_2}|}{\sqrt{\sigma_1^2 + \sigma_2^2}} \tag{9}$$

where $\overline{I_1}$ and $\overline{I_2}$ are the average intensities for several pixels in a bright region and in the background, respectively; and σ_1 and σ_2 are the corresponding standard deviations in these regions. We evaluate the CNR for quantum images generated from the same data set using a range of integration limits L, of the covariance peak for each pixel, in a pattern shown on Figure S3, where

$$QI_{\mathbf{k}} = \frac{1}{2}\left[\sum_{m=1}^{L} \mathrm{cov}(I_{\mathbf{k}}, I_{-\mathbf{k};m}) + \sum_{m=1}^{L} \mathrm{cov}(I_{-\mathbf{k}}, I_{\mathbf{k};m})\right]$$

Integrating beyond the center $-\mathbf{k}$ and $\mathbf{k}$ pixels at symmetric locations drastically improves the CNR, as more of the momentum correlation width is being integrated. We note that using $L = 1$, *i.e.*, generating the image from only the center covariance value, is equivalent to the method used by He et al.[19] The effects of integration limits on the CNR, computed for a range of the number of frames F used to generate each quantum image, are shown in Figure 3. We observe that for most values of F, $L = 21$ affords the greatest CNR. As the width of the $L = 21$ pattern is 5 pixels, and our momentum correlation width (MCW) is 5.2 pixels (See Figure S2), further increasing the integration limits beyond the MCW, would not be expected to improve the CNR. (Also, after approximately 500,000 frames, the CNR is not further improved, which may be attributable to shifting $\mathbf{k}$ and $-\mathbf{k}$ positions, *i.e.*, a shifting center of symmetry, at long acquisition time.) The greater CNR reported by He et al., obtained with $L = 1$ using the same number of frames, is attributable to their use of greater photon flux, and an SPDC wavelength for which the EMCCD has a higher quantum efficiency.[19]

RESULTS AND DISCUSSION

Achieving the Heisenberg Limit

Quantum imaging at the Heisenberg limit (HL) requires verifying the expected resolution improvement afforded by imaging with SPDC-photon pairs versus imaging with classical photons at the same wavelength. To verify that our SPDC images are at the HL, we measured the resolution of the image at the edge of an opaque object. We follow He et al.[19] by fitting an edge spread function (ESF):

https://doi.org/10.1021/acs.jpcb.6c03297
J. Phys. Chem. B 2026, 130, 10826−10835

Downloaded from pubs.acs.org/jpcbfk/article-pdf/130/41/10826/6872096/acs.jpcb.6c03297.pdf by IOWA STATE UNIV user on 15 October 2026

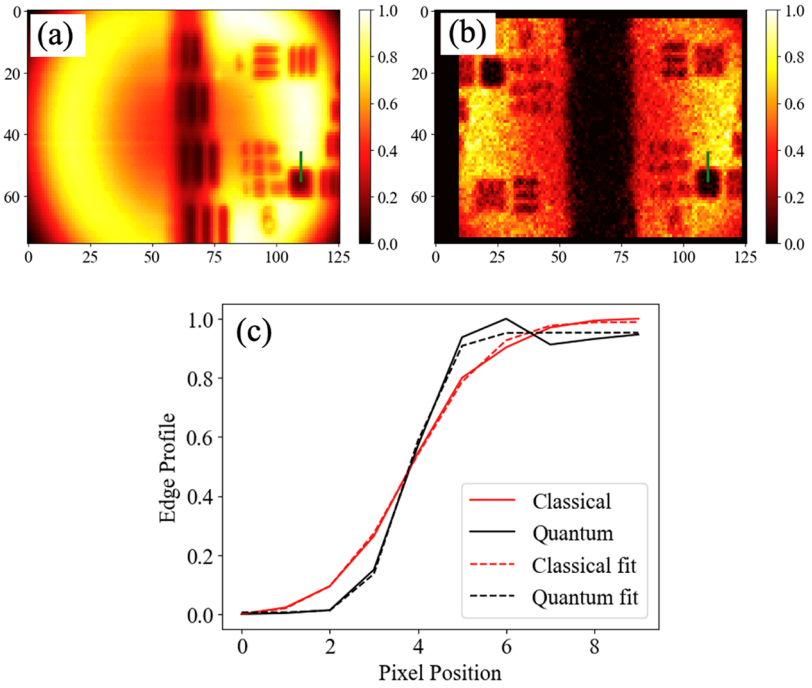


Figure 4. Testing the resolution of the system by measuring the profiles of the edge between a dark and illuminated region. Panel (a) presents the classical image; panel (b), the quantum image generated with the same data. In panels (a) and (b), the left-hand ordinates and abscissae are the pixel numbers. The green vertical line indicates the range of pixels used for one measurement. The classical and quantum image edge profiles along with their fits are presented in panel (c). The resolution is measured from $N = 3$ columns of pixels parallel to the green line. For the image shown, the classical-to-quantum image resolution ratio is 2.0 ± 0.2, demonstrating the Heisenberg limit.

$$\mathrm{ESF}(x) = a\mathrm{erf}\left(\frac{x - x_0}{w}\right) + b$$

where a and b are coefficients; x_0, the center of the edge; and w, the radius of the beam. This provides a Gaussian line spread function:

$$\mathrm{LSF}(x) = \frac{\mathrm{d}}{\mathrm{d}x}\mathrm{ESF}(x) = \frac{2a\exp\left[-\frac{(x-x_0)^2}{w^2}\right]}{w\sqrt{\pi}}$$

which allows us to obtain an estimated resolution: $R = 2\mathrm{w}\sqrt{(\ln(2))}$.

On a data set containing an opaque object (square box), we take a column of pixels perpendicular to the edge to determine the resolution for the classical and quantum images. For the classical image, we obtain $R_{810} = 3.4 \pm 0.1$ μm, and for the quantum image, $R_{\mathrm{QI}} = 1.7 \pm 0.2$ μm. Their ratio $\frac{R_{810}}{R_{\mathrm{QI}}} = 2.0 \pm 0.2$ demonstrates the HL, as shown in Figure 4. Errors are obtained from the standard deviation in R for $N = 3$ measurements. We note that the maximum improvement of the quantum measurement is not necessarily present at the alignment position where the resolution of the classical image is the best, necessitating the need for optimization shown in Figure S6.

Analysis of the Error of Measured Target Spacings, *s*

We refer to the Cramér-Rao lower bound (CRLB) in the Introduction. It has played a significant role in our approach to improving super-resolution measurements.[2] Thus, before undertaking the measurement of the spacings, s, of the USAF test chart, we calculated the CRLB for a series of targets with the corresponding slit separations. These calculations are briefly described in the SI, and the results are presented in Figure S7. The goal was not to attempt to attain quantitative agreement with Figure 6, which summarizes the experimental data below, but rather to predict—as indeed confirmed by experiment—that it is possible to perform measurements where the divergence of the error with decreasing s is slower than that of the classical measurements. Indeed, as observed, the quantum measurements afford standard deviations of the separations that deviate more slowly than those of the classical measurements as s is reduced.

With regard to the experiments, the data obtained from the targets of the USAF resolution test chart were fit to a function for generating a 2D image with an optical system modeled by a single thin lens[8]

$$\langle I(\overrightarrow{\rho_i})\rangle = A(\overrightarrow{\rho_o})^2 \otimes \mathrm{somb}^2\left[\mathrm{NA}\frac{2\pi}{\lambda}\left|\overrightarrow{\rho_o} + \frac{\overrightarrow{\rho_i}}{\mu}\right|\right] \quad (10)$$

NA is the numerical aperture of the optical system; μ, the magnification; λ, the wavelength of light; and ⊗ indicates convolution. $\overrightarrow{\rho_o}$ and $\overrightarrow{\rho_i}$ represent the vectors of the coordinates at the object and image planes, respectively. The point-spread function is $\mathrm{somb}(x) = \frac{2J_1(x)}{x}$, where $J_1(x)$ is the Bessel function of the first kind. (Equation 10 applies for an incoherent source, which provides a slightly better fit to the data than the corresponding equation[8] for a coherent source). The aperture function, eq 11, $A(\overrightarrow{\rho_o}) = A(s, w, x)$, is a product of a 1D step function that models the triple-bar targets of the 1951 USAF resolution test chart, whose bars and spacings of width s, are imaged by a beam of finite width, w

https://doi.org/10.1021/acs.jpcb.6c03297
J. Phys. Chem. B 2026, 130, 10826−10835

Downloaded from pubs.acs.org/jpcbfk/article-pdf/130/41/10826/6872096/acs.jpcb.6c03297.pdf by IOWA STATE UNIV user on 15 October 2026

$$A(s, w, x) = \begin{cases} 1, \text{ otherwise} \\ 0, \left(x < -\frac{w}{2}\right); \left(-\frac{5s}{2} < x < -\frac{3s}{2}\right); \\ \left(-\frac{s}{2} < x < \frac{s}{2}\right); \left(\frac{3s}{2} < x < \frac{5s}{2}\right); \left(\frac{w}{2} < x\right) \end{cases} \tag{11}$$

1 represents a bright region; 0, a dim region. A finite-width beam, broader than the triple-bar object ($w > 5s$), is required for a finite integral of $\langle I(\vec{\rho_i})\rangle$. A step-function approximates the relevant portion of the SPDC beam. Figure 5 presents an example for $A(s, w, x) = A(1.95\ \mu\text{m}, w, x)$.

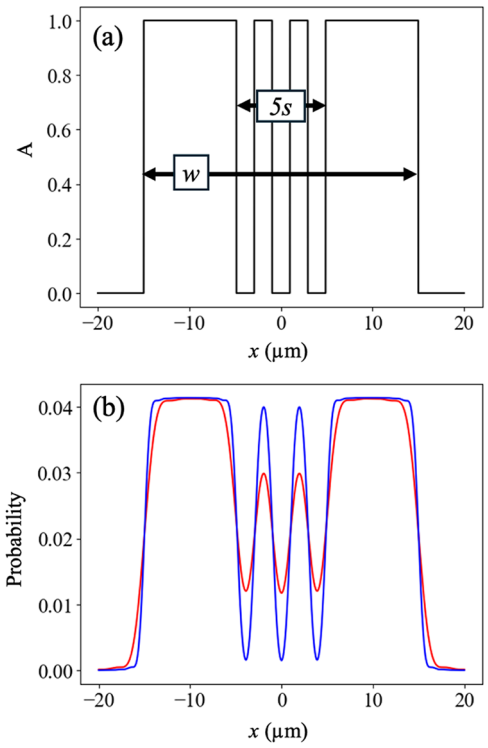


Figure 5. (a) $A(s, w, x)$ is the profile of a representative object being imaged before introduction into the single-lens image equation. A step-function beam of width 30 μm (held constant for all calculations) is blocked by the target, where each bar, and the gap between the bars, is equal to s, with the triple-bar object having a total width of $5s$. $A(1.95\ \mu\text{m}, 30\ \mu\text{m}, \text{x})$ is shown. (b) After introduction into the single-lens image, eq 10, the resulting intensity is normalized, yielding the probability distribution: $p(x,\text{NA},\lambda,\mu,s)$. With the NA and μ obtained from the data, $p(x,0.183, 405\text{ nm}, 1, 1.95\ \mu\text{m})$ (blue) and $p(x,0.183, 810\text{ nm}, 1, 1.95\ \mu\text{m})$ (red) are plotted.

The image function is converted to a probability distribution $p(x, \text{NA}, \lambda, \mu, s) = a\langle I(\vec{\rho_i})\rangle$ such that $\int_{-\infty}^{\infty} p(x,\text{NA},\lambda,\mu,s)\text{d}x = 1$, where a is a normalization constant. (Note, this normalization is not a "per-photon" normalization but a normalization of the probability distribution.) Fitting the size, s, requires knowledge of NA and μ, which were simultaneously fit by setting s to the size known to correspond to each triple-bar object on the 1951 USAF resolution test chart. For 3 representative bar sizes measured, $\mu = 28 \pm 1$ and NA = 0.183 ± 0.008 were measured. (As the objective lens has a nominal NA = 0.40, the lower value obtained from fitting is attributable to minor misalignment or positioning of the object slightly out of focus). The magnification is consistent with the optical arrangement of Figure 1. For a classical image containing images of several elements of the test chart, a box approximately 7 times the width of the bar on the 3-bar object is cropped around the object. The 1D profile of the image is taken by averaging the rows of pixels around the center line that comprise one-half the height of the cropped region (see Figure 6 and its caption). This is reasonable as the change in the y-profile of the image is minimal near the center of the triple-bar object. Profiles are converted to a probability distribution for fitting. The same region and procedure are used for the corresponding quantum images. Classical images are fit to $p(x,\text{NA},\lambda,\mu,s) = p(x,0.183, 810\text{ nm}, 28, s)$ and quantum images are fit to $p(x,\text{NA},\lambda,\mu,s) = p(x,0.183, 405\text{ nm}, 28, s)$. Fitting was performed in Python using least-squares regression. The s intervals used for fitting are less than 0.003 μm, which are well within the error measured for the largest bar investigated ($s = 1.75\ \mu$m).

For bars on a quantum image, the standard deviation in the fitted size for $N = 21$ images is divided by the average measured size of each element on the resolution test chart to yield a relative error. The number of frames F used to generate each image on which the size was measured was selected to ensure an equal number of 810 nm classical photons and SPDC photon pairs used to generate the classical and quantum images, respectively, based on the measured quantum efficiency (described in Experimental Methods section and SI). Classical images are created by summing frames that are taken at evenly spaced intervals during the acquisition of a larger number of frames required to generate the quantum image. This ensures that any shift in the target affects both the classical and quantum images equally. The full classical images, which include signal and idler beams (example in Figure 6(a)), have an overall mean flux of 0.1045 ± 0.0005 photons/pixel after application of the threshold. This is equivalent to $1000. \pm 5$ photons/frame, considering the dimensions of our frame. For the regions cropped around each of the measured three-bar objects (example in Figure 6(b)), we have a mean flux of 0.119 ± 0.005 on a representative data set. Considerable attention was paid to verify that N and F are each sufficiently large so that the distribution of measurements for each bar size yielding the standard deviations reported in Figure 6 is attributable primarily to the inherent uncertainty in measuring the object (due to movement of the object, unavoidable noise, photon spread, *etc.*) rather than from noisy images whose image quality is limited by the integration time used for the acquisition (*i.e.* the number of photons on the image). The rationale justifying the selection of N and F is discussed further in the SI.

CONCLUSIONS

This is another step in our attempt to develop a method of attaining super-resolution with nonblinking sources. Clearly, however, demonstrating the Heisenberg limit for micron-sized targets is a far cry from resolving molecules with tens-of-nanometer precision.[3] But by developing a refined, robust method of covariance analysis and determining the precision of the measurements of a series of nonpoint-source targets, as well as the trends in the Cramér-Rao lower bound, we propose that this work lays a firm basis for moving forward in the context of our previous efforts, notably those using interference to achieve super-resolution in heterodyning experiments.[2] The CRLB is fundamental in our thinking about the problem of super-resolution for nonpoint sources. While the point-spread function provides an effective means of characterizing the

Downloaded from pubs.acs.org/jpcbfk/article-pdf/130/41/10826/6872096/acs.jpcb.6c03297.pdf by IOWA STATE UNIV user on 15 October 2026

https://doi.org/10.1021/acs.jpcb.6c03297
J. Phys. Chem. B 2026, 130, 10826−10835

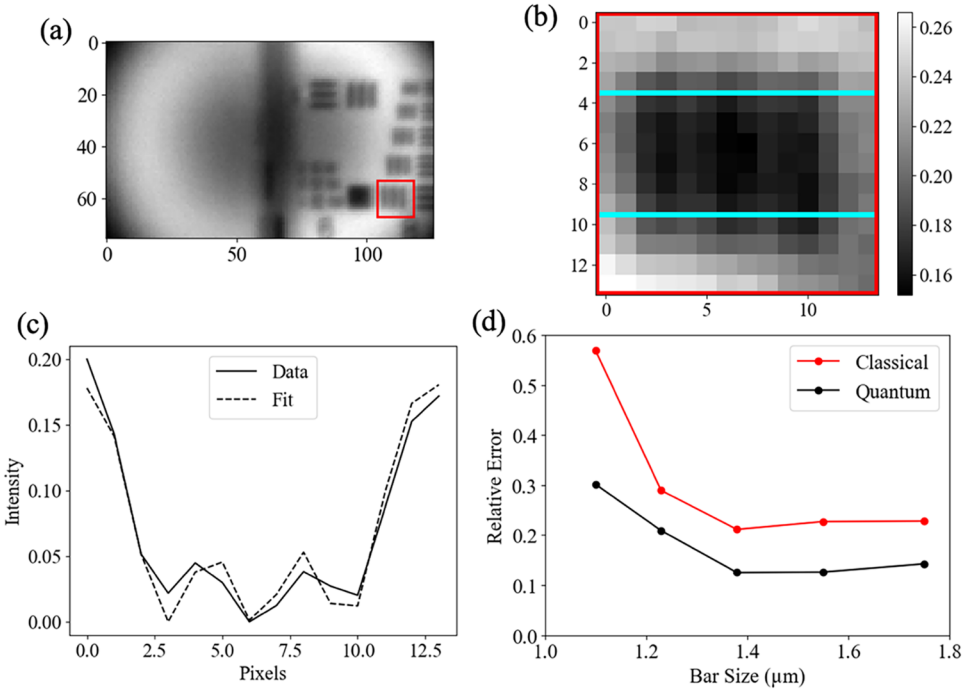


Figure 6. Comparison in the error of the size measurement as determined from classical (red) and quantum (black) measurements. (a) The image before the covariance analysis. The image of the $s = 1.75$ μm object from Group 8 of the resolution test chart is outlined in red. (b) Detail of panel (a) showing the image of a target with $s = 1.75$ μm, cropped from the red box in (a). (c) Fit of the image through a horizontal line going through the center of the target, generated from averaging the columns contained between the cyan lines on (b). The horizontal profiles of the targets are fit to $p(x,\mathrm{NA},\lambda,\mu,s)$ The fitting was performed for $N = 21$ experiments (*i.e.*, images), each of 39,318 frames for the raw data (classical imaging) and 750,000 frames for the quantum images. The number of frames/images is determined so that the number of classical, 810 nm photons and entangled, SPDC pairs contributing to each image is equivalent. The standard deviation in the measurement of each size is divided by the average measured size to yield a relative error. (d) Comparison of the error in the classical and quantum measurements as a function of bar size, s. This panel presents a fundamental result of the work. Namely, it demonstrates the slowing down of the divergence of the error of the measurement of progressively smaller slit separations for the quantum with respect to the classical measurement.

accuracy of the imaging of point sources, a realistic object is an infinite number of point sources. The CRLB is more general than the PSF, going well beyond it by providing an efficient and effective means of characterizing parameters that are *not* point sources.

The characterization of the resolution of a point source employs the appropriately named "point-spread function," the PSF. The width of the PSF can be identified as the CRLB of the position parameter of the point source. This CRLB is determined by the probability distribution of *one measurement*. For point-source imaging, the diffraction limit is the same as the CRLB of the position parameter of the point source. Naturally if N *identically* repeated measurements are performed, one can measure the position of the point source with an accuracy better than the diffraction limit. And, indeed, performing such repeated measurements is the foundation of fluorescence-based, subdiffraction imaging methods.[3] In reality, however, it is well-known that N cannot be made arbitrarily large because of, for example, irreversible photobleaching and degradation of the fluorescent probe.

A point-spread function can obviously not be employed for determining the accuracy of the imaging of a nonpoint source, a "realistic" object. It is both impractical and unreasonable to try to approximate a nonpoint source object as large sum of point sources. *It is necessary to use the CRLB of the parameter (or parameters) characterizing the object, which is our case is the slit size*. To define "a measurement" for such an imaging process requires, however, considerable effort, which we describe in detail in Figure S5 and its caption. The theoretical CRLB in our case is defined by one measurement's probability distribution, namely "an image integrating to 1," which we present in Figure 5 of the manuscript. Since there is no way to find this "theoretical CRLB" directly from experimental measurements, at least to our knowledge, we obtained the standard deviation of N repeated measurements via experiments (Figure 6d). Such a direct comparison between the "theoretical CRLB" and the experimentally measured standard deviation is challenging given the various approximations involved. (In our previous paper involving classical imaging,[2] we did such a comparison with realistic noise models, but with only partial success. For the current quantum imaging case, we felt that the comparison for the trend is justified to illustrate the advantage of quantum imaging).

In this context, the seminal work of Hong, Ou, and Mandel[23] (HOM) enables a strategy: the interference of the amplitudes of entangled signal-idler pairs may slow down the divergence of the CRLB significantly more than that observed in the present work. Parniak et al.[16] achieved promising experimental and computational results for a simple model system for which they computed the qCRLB and performed HOM interferometry. They were successful in retarding the divergence of their observed error. Devaux and co-workers[17,18] performed a detailed exploration of the spatial interference in a more complicated system that elucidated the multimode structure of entangled photons, suggesting a pathway to enhanced resolution and, perhaps, super resolution.

https://doi.org/10.1021/acs.jpcb.6c03297
J. Phys. Chem. B 2026, 130, 10826−10835

Downloaded from pubs.acs.org/jpcbfk/article-pdf/130/41/10826/6872096/acs.jpcb.6c03297.pdf by IOWA STATE UNIV user on 15 October 2026

■ ASSOCIATED CONTENT

Supporting Information

The Supporting Information is available free of charge at https://pubs.acs.org/doi/10.1021/acs.jpcb.6c03297.

Calibration results (Figure S1) and details of photon number calculation; momentum correlation width (Figure S2); description of center of inversion symmetry algorithm; covariance peak integration diagram (Figure S3); image used for CNR calculation (Figure S4); convergence in the error in the measurement of bar sizes with respect to parameters affecting the number of photons used (Figure S5) and discussion; optimization of the focus and the Heisenberg limit (Figure S6); CRLB calculation for a triple-bar object imaged with a single lens (Figure S7) (PDF)

■ AUTHOR INFORMATION

Corresponding Authors

Jacob W. Petrich − *Department of Chemistry, Iowa State University, Ames, Iowa 50011, United States; Ames National Laboratory, U.S. Department of Energy, Ames, Iowa 50011, United States;* orcid.org/0000-0001-9527-6832; Email: jwp@iastate.edu

Xueyu Song − *Department of Chemistry, Iowa State University, Ames, Iowa 50011, United States; Ames National Laboratory, U.S. Department of Energy, Ames, Iowa 50011, United States;* orcid.org/0000-0001-5142-4223; Email: xsong@iastate.edu

Authors

Dorian F. Twedt-Gutierrez − *Department of Chemistry, Iowa State University, Ames, Iowa 50011, United States; Ames National Laboratory, U.S. Department of Energy, Ames, Iowa 50011, United States;* orcid.org/0009-0002-3843-1458

Emily A. Smith − *Department of Chemistry, Iowa State University, Ames, Iowa 50011, United States; Ames National Laboratory, U.S. Department of Energy, Ames, Iowa 50011, United States;* orcid.org/0000-0001-7438-7808

Complete contact information is available at: https://pubs.acs.org/10.1021/acs.jpcb.6c03297

Notes

The authors declare no competing financial interest.

■ ACKNOWLEDGMENTS

This material is based upon work supported by the Ames National Laboratory's Laboratory Directed Research and Development (LDRD) program and by the Air Force Office of Scientific Research under award number FA9550-23-1-0591.

■ REFERENCES

(1) Singh, A. K.; Santra, K.; Song, X.; Petrich, J. W.; Smith, E. A. Spectral Narrowing Accompanies Enhanced Spatial Resolution in Saturated Coherent Anti-Stokes Raman Scattering (CARS): Comparisons of Experiment and Theory. *J. Phys. Chem. A* **2020**, *124* (21), 4305−4313.

(2) Santra, K.; Nguyen, V.; Smith, E. A.; Petrich, J. W.; Song, X. Localization of Nonblinking Point Sources Using Higher-Order-Mode Detection and Optical Heterodyning: Developing a Strategy for Extending the Scope of Molecular, Super-Resolution Imaging. *J. Phys. Chem. B* **2021**, *125* (12), 3092−3104.

(3) Von Diezmann, L.; Shechtman, Y.; Moerner, W. E. Three-Dimensional Localization of Single Molecules for Super-Resolution Imaging and Single-Particle Tracking. *Chem. Rev.* **2017**, *117* (11), 7244−7275.

(4) Yonemaru, Y.; Palonpon, A. F.; Kawano, S.; Smith, N. I.; Kawata, S.; Fujita, K. Super-Spatial- and -Spectral-Resolution in Vibrational Imaging via Saturated Coherent Anti-Stokes Raman Scattering. *Phys. Rev. Appl.* **2015**, *4* (1), No. 014010.

(5) Tsang, M.; Nair, R.; Lu, X.-M. Quantum Theory of Superresolution for Two Incoherent Optical Point Sources. *Phys. Rev. X* **2016**, *6* (3), No. 031033.

(6) Helstrom, C. W. *Quantum Detection and Estimation Theory*; Academic Press:: New York, 1976.

(7) van den Bos, A. *Parameter Estimation for Scientists and Engineers*; Wiley-Interscience:: Hoboken, N.J, 2007 DOI: 10.1002/9780470173862.

(8) Shih, Y. *An Introduction to Quantum Optics: Photon and Biphoton Physics*, 2nd ed.; CRC Press, Taylor & Francis Group:: Boca Raton, 2021.

(9) Defienne, H.; Ndagano, B.; Lyons, A.; Faccio, D. Polarization Entanglement-Enabled Quantum Holography. *Nat. Phys.* **2021**, *17* (5), 591−597.

(10) Defienne, H.; Reichert, M.; Fleischer, J. W. Adaptive Quantum Optics with Spatially Entangled Photon Pairs. *Phys. Rev. Lett.* **2018**, *121* (23), No. 233601.

(11) Moreau, P.-A.; Toninelli, E.; Morris, P. A.; Aspden, R. S.; Gregory, T.; Spalding, G.; Boyd, R. W.; Padgett, M. J. Resolution Limits of Quantum Ghost Imaging. *Opt. Express* **2018**, *26* (6), 7528−7536.

(12) Gregory, T.; Moreau, P.-A.; Toninelli, E.; Padgett, M. J. Imaging through Noise with Quantum Illumination. *Sci. Adv.* **2020**, *6* (6), No. eaay2652.

(13) Unternährer, M.; Bessire, B.; Gasparini, L.; Perenzoni, M.; Stefanov, A. Super-Resolution Quantum Imaging at the Heisenberg Limit. *Optica* **2018**, *5* (9), 1150−1154.

(14) Jachura, M.; Chrapkiewicz, R.; Demkowicz-Dobrzański, R.; Wasilewski, W.; Banaszek, K. Mode Engineering for Realistic Quantum-Enhanced Interferometry. *Nat. Commun.* **2016**, *7* (1), No. 11411.

(15) Jachura, M.; Chrapkiewicz, R. Shot-by-Shot Imaging of Hong−Ou−Mandel Interference with an Intensified sCMOS Camera. *Opt. Lett.* **2015**, *40* (7), 1540−1543.

(16) Parniak, M.; Borówka, S.; Boroszko, K.; Wasilewski, W.; Banaszek, K.; Demkowicz-Dobrzański, R. Beating the Rayleigh Limit Using Two-Photon Interference. *Phys. Rev. Lett.* **2018**, *121* (25), No. 250503.

(17) Devaux, F.; Mosset, A.; Lantz, E. Stochastic Numerical Simulations of a Fully Spatiotemporal Hong-Ou-Mandel Dip. *Phys. Rev. A* **2019**, *100* (1), No. 013845.

(18) Devaux, F.; Mosset, A.; Moreau, P.-A.; Lantz, E. Imaging Spatiotemporal Hong-Ou-Mandel Interference of Biphoton States of Extremely High Schmidt Number. *Phys. Rev. X* **2020**, *10* (3), No. 031031.

(19) He, Z.; Zhang, Y.; Tong, X.; Li, L.; Wang, L. V. Quantum Microscopy of Cells at the Heisenberg Limit. *Nat. Commun.* **2023**, *14* (1), No. 2441.

(20) Klyshko, D. N. Use of Two-Photon Light for Absolute Calibration of Photoelectric Detectors. *Sov. J. Quantum Electron.* **1980**, *10* (9), 1112−1117.

(21) Meda, A.; Ruo-Berchera, I.; Degiovanni, I. P.; Brida, G.; Rastello, M. L.; Genovese, M. Absolute Calibration of a Charge-Coupled Device Camera with Twin Beams. *Appl. Phys. Lett.* **2014**, *105* (10), No. 101113.

(22) Avella, A.; Ruo-Berchera, I.; Degiovanni, I. P.; Brida, G.; Genovese, M. Absolute Calibration of an EMCCD Camera by Quantum Correlation, Linking Photon Counting to the Analog Regime. *Opt. Lett.* **2016**, *41* (8), 1841−1844.

Downloaded from pubs.acs.org/jpcbfk/article-pdf/130/41/10826/6872096/acs.jpcb.6c03297.pdf by IOWA STATE UNIV user on 15 October 2026

(23) Hong, C. K.; Ou, Z. Y.; Mandel, L. Measurement of Subpicosecond Time Intervals between Two Photons by Interference. *Phys. Rev. Lett.* **1987**, *59* (18), 2044−2046.

Downloaded from pubs.acs.org/jpcbfk/article-pdf/130/41/10826/6872109 6/acs.jpcb.6c03297.pdf by IOWA STATE UNIV user on 15 October 2026

https://doi.org/10.1021/acs.jpcb.6c03297
J. Phys. Chem. B 2026, 130, 10826−10835

Supporting Information

Comparison of the Error Incurred in the Measurement of Nonblinking, Nonpoint-source Objects Using Classical and Quantum Imaging

Dorian F. Twedt-Gutierrez, Emily A. Smith, Jacob W. Petrich*, and Xueyu Song*

Department of Chemistry, Iowa State University, Ames, Iowa 50011

Ames Laboratory, U.S. Department of Energy, Ames, Iowa 50011

* To whom correspondence should be addressed.

dtwedt@iastate.edu, esmith1@iastate.edu, jwp@iastate.edu, xsong@iastate.edu

Downloaded from pubs.acs.org/jpcbfk/article-supplement/5443067/pdf/jp6c03297_si_001/ by guest on 01 October 2026

Calibration of the Number of Classical and Entangled Photons

$P_{\mathrm{NC}}(T)$, introduced in the main text, is the probability of a pixel reporting a noise count at a threshold T without laser illumination. After obtaining $P_{\mathrm{NC}}(T)$, we calibrated the EMCCD *in situ* using photon pairs generated by spontaneous parametric down-conversion (SPDC) using the experimental apparatus of **Figure 1** of the main text. The procedure is informed by the absolute calibration method employed by Meda *et al.*[1] and Avella *et al*.[2] A crucial difference between our procedure and theirs, however, is that ours uses the same optical configuration as that of the imaging experiment. This ensures that the measured $\eta(T)$ incorporates both the intrinsic detector quantum efficiency and all transmission losses in the optical path.[2] The EMCCD was operated under the same conditions as those described in Methods. For purposes of this calibration, we assume the detector is operated under conditions of at most one photon per pixel per frame.

The EMCCD output signal, n_{e^-} (counts/pixel), can be modeled as the sum of amplified photoelectron events and noise contributions.[1,2] In the absence of illumination, the measured distribution $P_{\mathrm{NC}}(T)$ is determined by Gaussian readout noise and spurious charges (clock-induced charge, CIC), which are amplified by electron multiplication. To obtain $P_{\mathrm{NC}}(T)$, we acquired 10 frames with the EMCCD detector shutter closed, using the same acquisition parameters used to acquire SPDC data used for classical and quantum imaging. For a range of T values above the bias of the Gaussian readout noise, the threshold condition [$n_{e^-} \geq T \rightarrow 1$ ("click"); $n_{e^-} < T \rightarrow 0$] is applied. $P_{\mathrm{NC}}(T)$ is the fraction of pixels with value 1. $P_{\mathrm{NC}}(T)$ is computed for a range of thresholds, yielding the curve shown in **Figure S1**. The inflection point in the curve is the transition between the Gaussian readout noise distribution and the exponential distribution of electron-multiplied spurious counts.[2] Because the quantum efficiency, $\eta(T)$, decreases as a function of threshold,[2] selecting a threshold value at the inflection point of **Figure S1** offers a high quantum efficiency

Downloaded from pubs.acs.org/jpcbfk/article-supplement/5443067/pdf/jp6c03297_si_001/ by guest on 01 October 2026

and a sufficiently low number of noise clicks due to spurious counts, before the noise probability approaches unity as T is further decreased. We selected $T = 525$, which is just before the inflection point where $P_{\mathrm{NC}}(T)$ begins to increase sharply as T decreases. $T = 525$ is used for imaging throughout, where $P_{\mathrm{NC}}(525) = 0.0050$. We note that $P_{\mathrm{NC}}(T)$ only accounts for read noise in the absence of light, and neglects other sources of noise, such as stray light not contributing to the image.

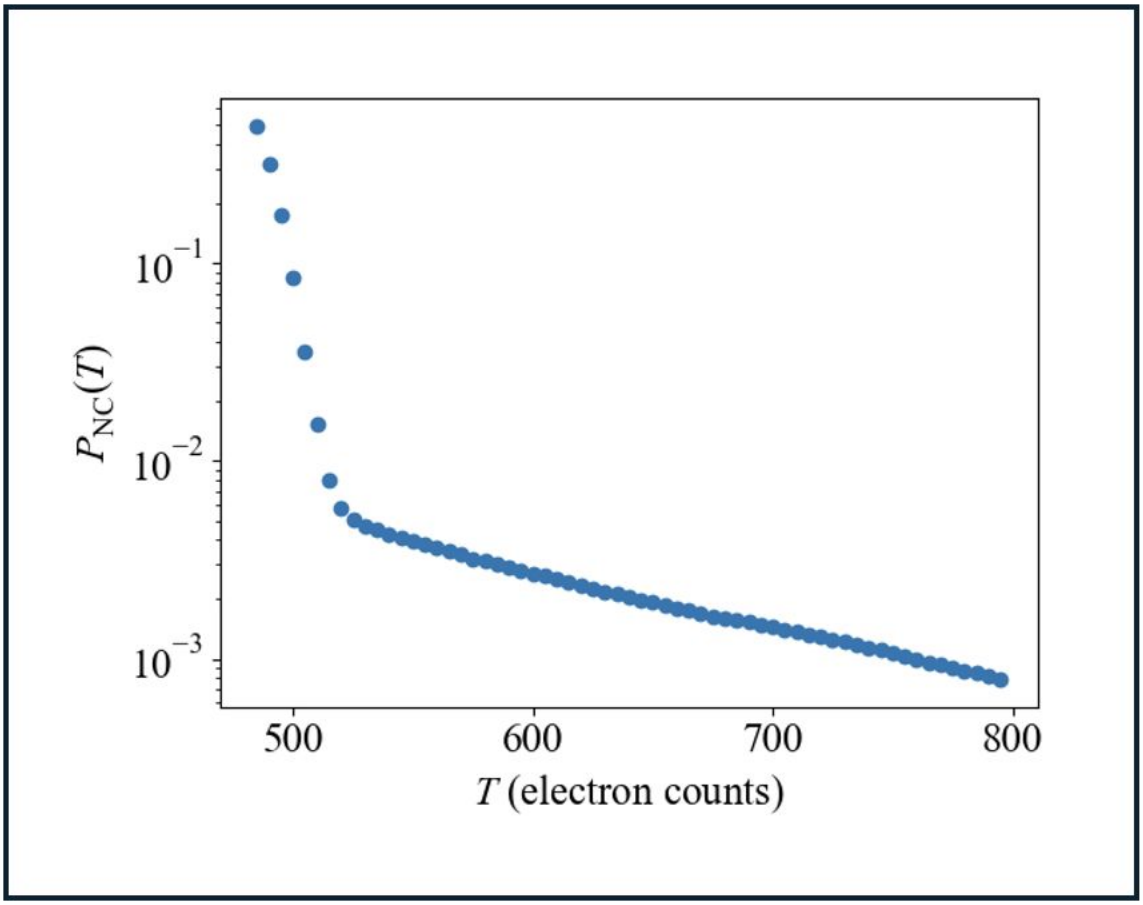


Figure S1. Noise calculation. The probability of a noise count as a function of threshold $P_{\mathrm{NC}}(T)$ is computed for a range of thresholds for 10 dark frames taken with the EMCCD shutter closed. Following Avella *et al.*[2], the quantum efficiency is maximized at the inflection point of $P_{\mathrm{NC}}(T)$. $T = 525$ is used for the images we present.

Downloaded from pubs.acs.org/jpcbfk/article-supplement/5443067/pdf/jp6c03297_si_001/ by guest on 01 October 2026

Quantum Efficiency from SPDC Correlations

The threshold-dependent quantum efficiency, $\eta(T)$, is determined using spatial correlations between signal and idler photons generated by SPDC. Having selected the value T that offers the optimal quantum efficiency, a quantum image was generated using the method described in the main text, and a **k** and **-k** pair was selected from an area of the image not obscured by an object on the resolution test chart. (The resolution test chart was not removed during the calibration to maintain the integrity of the optical path.) The 21-pixel regions centered at **k** and **-k** were used as the regions N_s and N_i, corresponding to those arising from the signal and the idler respectively, for the correlation analysis used to determine $\eta(T)$. Following Meda and coworkers[1], we quantify the spatial correlations using the covariance:

$$C = \langle N_s N_i \rangle - \langle N_s \rangle \langle N_i \rangle, \tag{S1}$$

which isolates the contribution from photon-pair correlations by subtracting uncorrelated background fluctuations. The covariance calculation is the same as that used for quantum imaging. In the photon-counting regime (at most one photon per pixel per frame), this covariance is proportional to the product of the detection efficiency and the mean photon number in the reference area. The quantum efficiency, $\eta(T)$, is obtained from SPDC correlations in a manner first described by Klyshko[3] and adapted by Meda *et al.*,[1] with

$$\eta(T) = C/A\langle N_{\mathrm{ref}} \rangle, \tag{S2}$$

where $\langle N_{\mathrm{ref}} \rangle$ is either $\langle N_s \rangle$ or $\langle N_i \rangle$, which are assumed to be equal owing to the symmetric configuration used (**Figure 1**) and is obtained from the average intensity over several bright pixels. We obtain C by integrating a 21-pixel region for a known **k** and **-k** pair from a representative data set. The quantities N_s, N_i, and C are accumulated over 1.5 million frames and are obtained after having applied the selected threshold, T. A is a geometric parameter, which we take to be 1, as *only*

Downloaded from pubs.acs.org/jpcbfk/article-supplement/5443067/pdf/jp6c03297_si_001/ by guest on 01 October 2026

the covariance peak is integrated to give *C*. The number of true counts used for $\langle N_{\mathrm{ref}} \rangle$ is corrected for noise using $N_{\mathrm{true}} = N_{\mathrm{click}} - N_{\mathrm{noise}}$, with N_{noise} determined from $N_{\mathrm{noise}} = N_{\mathrm{click}} P_{\mathrm{NC}}(T)$. We find $\eta(525) = 0.052$. As noted above, this efficiency represents the *total* system detection efficiency, including both optical losses and the intrinsic EMCCD quantum efficiency. As the EMCCD itself is specified by the manufacturer to have a quantum efficiency of ~70% at 810 nm, an efficiency of 5.2% suggests the majority of losses occur along the imaging path, which is reasonable for the system presented in **Figure 1**.

Momentum Correlation Width

Determining the width of the peak in covariance values is necessary for assessing the probability distribution for finding the twin of a given entangled pair. It is also necessary for determining the integration boundaries (*L*) used to generate the quantum image, as described in the main text. For each pixel located at $\mathbf{k} = (i, j)$, we observe a Gaussian peak of covariance values (spanning multiple pixels), centered at the symmetric location $-\mathbf{k} = (k,l)$. We equate the width of this Gaussian to the momentum correlation width (MCW) or, equivalently, to the joint probability distribution of the signal and idler.

To find the MCW for each pixel, $\mathbf{k} = (i,j)$, a scan is performed to determine the location (k,l) of the cluster of covariance values with the highest value. The location of the peak is found by determining the coordinates (k,l) that gives the maximum value of $\sum_{m=1}^{9} \mathrm{cov}\left(I_{\mathbf{k}}, I_{-\mathbf{k};\, m}\right)$, where 9 pixels including and surrounding the coordinate (k,l):

$$\mathrm{peak}_{\mathbf{k}} = (k,l) = \max_{k,l} \sum_{m=1}^{9} \mathrm{cov}\left(I_{\mathbf{k}}, I_{(k,l);\, m}\right). \tag{S3}$$

For each pixel $\mathbf{k} = (i,j)$, on the right side of the image, the scan is performed only on the left side of the image and *vice versa*, as we know that due to the optical arrangement, the covariance peak from an entangled photon on one side will be present only on the opposite side. Pixels near the

Downloaded from pubs.acs.org/jpcbfk/article-supplement/5443067/pdf/jp6c03297_si_001/ by guest on 01 October 2026

boundaries of the image, where a peak would be incomplete, are ignored while scanning. Identifying the 3x3 cluster of 9 pixels that together have the highest integral covariance value is superior to finding only the highest covariance value pixel, since performing the integral of 9 pixels averages the noise present in the distribution and is more likely to identify the exact center of the covariance peak at (k,l). This is because, owing to the relatively low signal-to-noise ratio of the peaks in the covariance matrix, the pixel with the highest value may not be at the center of the Gaussian peak.

The scan finds a peak in covariance values for all **k** locations, *even those with no entangled photons*, in which case the found "peak" will correspond to a random location with slightly higher correlated noise. To build the MCW, we take the 3126 pixels with the highest peak integrals, which all have source pixels **k** located on the brightly illuminated portion of the quantum image. The covariance matrix used for obtaining the MCW is a representative data set used for quantum imaging. The values of the covariance matrix at the center of the found peak (**-k**) are averaged and normalized to yield the MCW for the experiment. The centerline of the MCW is fit to a Gaussian, and a full-width at half-maximum (FWHM) of the fit has a width of 5.2 pixels (**Figure S2a**). The Gaussian tails of the MCW distribution, which extend beyond the 3x3 pixels used for the initial scan, affirm that the scanning method is effective at locating the center of a distribution that is broader than the 3x3 pixel area used for the scan. Converting to length using the pixel width of 26 μm/pixel and scaling by the observed magnification between the object plane and the detector (μ = 28) results in an estimated MCW of 4.9 μm at the object plane. (A source of error in the MCW is that the pixels, notably the center pixel, has finite width of 26 μm and is not a point source.)

Downloaded from pubs.acs.org/jpcbfk/article-supplement/5443067/pdf/jp6c03297_si_001/ by guest on 01 October 2026

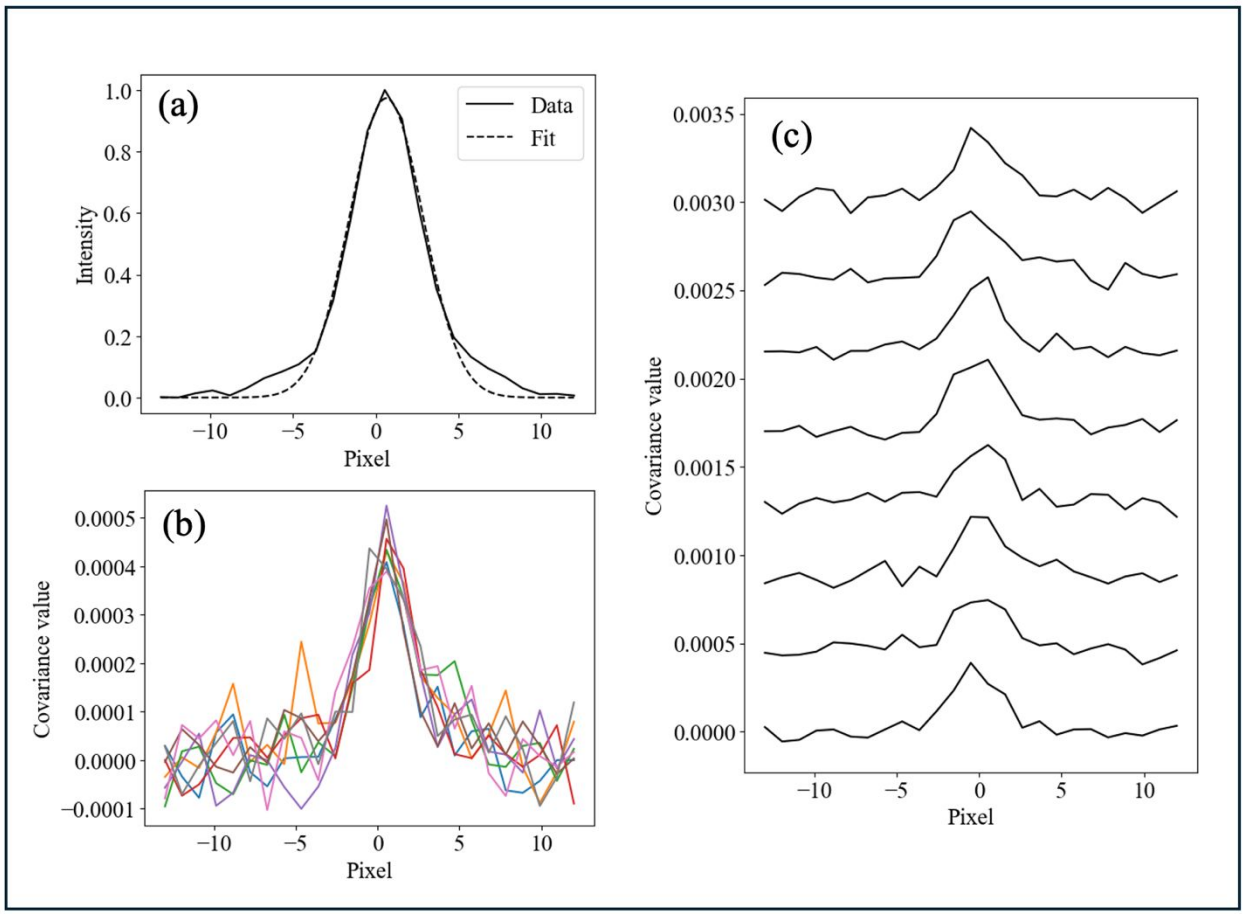


Figure S2. Momentum correlation width.

(a) Sum of horizontal covariance values, centered on the 9-pixel covariance peak, for pixels from the illuminated portion of a quantum image (N = 3126 pixels), to compute the MCW. A Gaussian fit yields a FWHM = 5.2 pixels.

(b) Average of horizontal and vertical profiles of eight **k** and –**k** peak locations. (c) The profiles are overlapped and displaced to facilitate viewing.

Downloaded from pubs.acs.org/jpcbfk/article-supplement/5443067/pdf/jp6c03297_si_001/ by guest on 01 October 2026

Finding k and -k and Generating the Quantum Image

To locate the coordinates of **-k** corresponding to a given **k** = (*i,j*), an initial-guess position is made by picking the image coordinates at the symmetric position about the center of the image. For an image with dimensions $d_x \times d_y$, the guessed position is $-\mathbf{k}_{\text{guess}} = (d_x - i, d_y - j)$. A scan is performed to determine the location (k,l) of the cluster of covariance values with the highest value. The location of the peak is found by determining the coordinates (k,l) that gives the maximum value of $\sum_{m=1}^{9} \text{cov}\left(I_{\mathbf{k}}, I_{-\mathbf{k};\, m}\right)$, where m are the 9 pixels including and surrounding the coordinate (k,l).

$$\text{peak}_{\mathbf{k}} = (k,l) = \max_{k,l} \sum_{m=1}^{9} \text{cov}\left(I_{\mathbf{k}}, I_{(k,l);\, m}\right). \tag{S4}$$

For a **k** and **-k** pair corresponding to a clear, symmetric SPDC beam path (undisturbed by the object), $\text{peak}_{\mathbf{k}} = -\mathbf{k}$. As the found peak coordinates are only valid for the regions of the beam that have the covariance peaks with the highest signal-to-noise ratio, a cutoff is chosen as the ~100 pixels with the highest $\text{cov}(I_{\mathbf{k}}, I_{-\mathbf{k}})$ values. For the peaks above the cutoff, the average difference between the guessed coordinate $-\mathbf{k}_{\text{guess}}$ and $\text{peak}_{\mathbf{k}}$ is used to generate an offset applied for all other **k** positions.

$$(\text{offset}_x, \text{offset}_y) = (k,l)_{-\boldsymbol{k}_{\text{guess}}} - (k,l)_{\text{peak}_{\boldsymbol{k}}} \tag{S5}$$

The offsets are computed from enough of the brightest **k** and **-k** pairs with $\text{cov}(I_{\mathbf{k}}, I_{-\mathbf{k}})$ values above the cutoff value to ensure that we have a unique center of symmetry, as indicated by the individual pixels above the cutoff returning the same offsets, within approximately one pixel. The offsets are then used to find the **-k** position corresponding to each pixel **k** = (*i, j*)

$$-\mathbf{k} = (d_x - i + \text{offset}_x, d_y - j + \text{offset}_x) \tag{S6}$$

Downloaded from pubs.acs.org/jpcbfk/article-supplement/5443067/pdf/jp6c03297_si_001/ by guest on 01 October 2026

149 The result of this procedure is to extrapolate **k** and -**k** coordinate locations for regions where no
150 covariance peak is located, *i.e.*, where the beam is not present, or one of the biphotons was scattered
151 away by the object.

152 This algorithm allows automatic generation of a quantum image without the need for
153 precise mechanical alignment of the beam path. Nor does it require "manual" alignment of left and
154 right panels in software. It also corrects for shifting beam paths. It is conceivable that another
155 factor contributing to the asymmetry between left and right optical paths arises from slight
156 variations due to imperfect positioning of the optical components. This could produce asymmetric
157 paths between signal and idler as well as different magnification in the object- and reference-beam
158 paths. Also, one or both of these two beam paths may be slightly rotated perpendicular to the z
159 plane about some (x, y) position. Our algorithm does not correct for this, as we observe that these
160 shifts are smaller than the width of the observed joint probability distribution. If, however, the left
161 and right beams were significantly skewed, the peak-finding algorithm could be modified to
162 correct for distortions in other degrees of freedom.
163

Downloaded from pubs.acs.org/jpcbfk/article-supplement/5443067/pdf/jp6c03297_si_001/ by guest on 01 October 2026

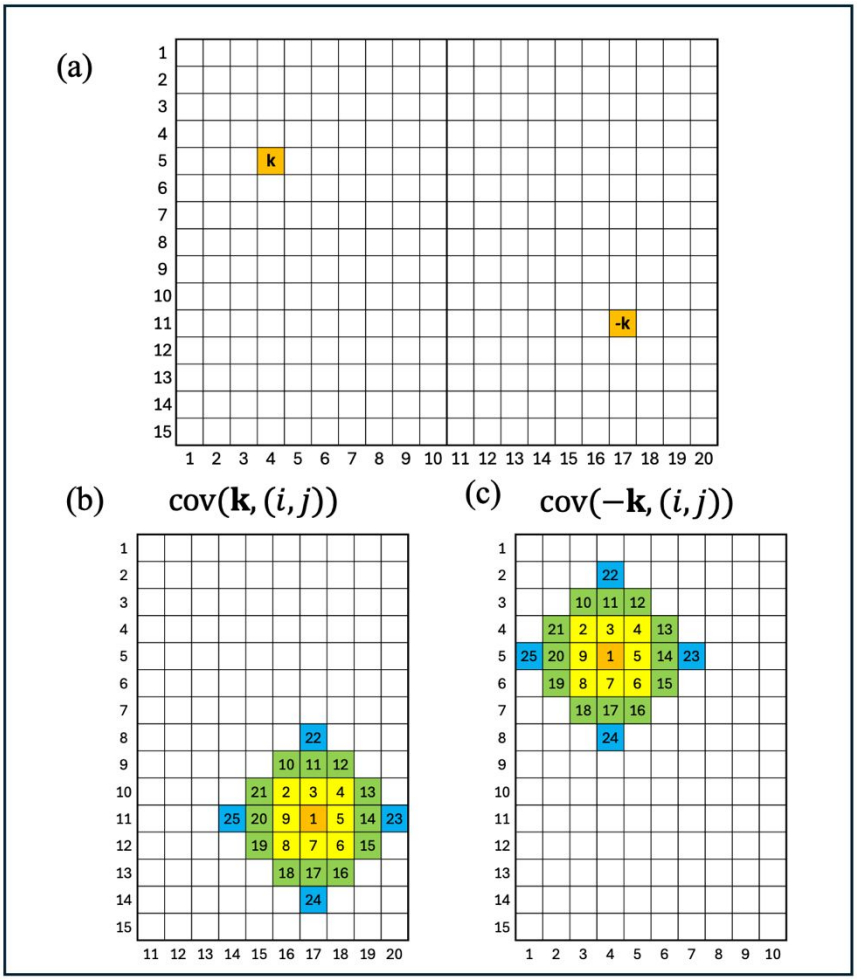


Figure S3. Covariance matrix integration limits for an example data set with dimensions 20 x 15 pixel^2.

(a) The original image dimensions, with an example **k** at pixel (4,5). Assuming offsets are 0, **-k** is at the symmetric position, (17,11).
(b) The right half of the 2D covariance matrix cov(**k**,(*i*,*j*)). L = 21 values of the pixels of the covariance peak centered at the symmetric position, –**k** = (17,11) in panel c, are summed: $\sum_{m=1}^{L} \mathrm{cov}\left(I_{\mathbf{k}}, I_{-\mathbf{k};\, m}\right)$.
(c) The left half of the 2D covariance matrix cov(−**k**,(*i*,*j*)). L = 21 values of the pixels of the covariance peak centered at the symmetric position, **k** = (4,5) in panel b, are summed: $\sum_{m=1}^{L} \mathrm{cov}\left(I_{-\mathbf{k}}, I_{\mathbf{k};\, m}\right)$. The final quantum image intensity at the example pixel **k** is given by Eq 8, reproduced here:

$$QI_{\mathbf{k}} = \frac{1}{2}\left[\sum_{m=1}^{L} \mathrm{cov}\left(I_{\mathbf{k}}, I_{-\mathbf{k};\, m}\right) + \sum_{m=1}^{L} \mathrm{cov}\left(I_{-\mathbf{k}}, I_{\mathbf{k};\, m}\right)\right].$$

The opposite halves of the 2D covariance matrices (panels b and c) are not shown, as the covariance peak is always on the opposite half of the image plane, owing to the symmetry of the experimental setup.

Downloaded from pubs.acs.org/jpcbfk/article-supplement/5443067/pdf/jp6c03297_si_001/ by guest on 01 October 2026

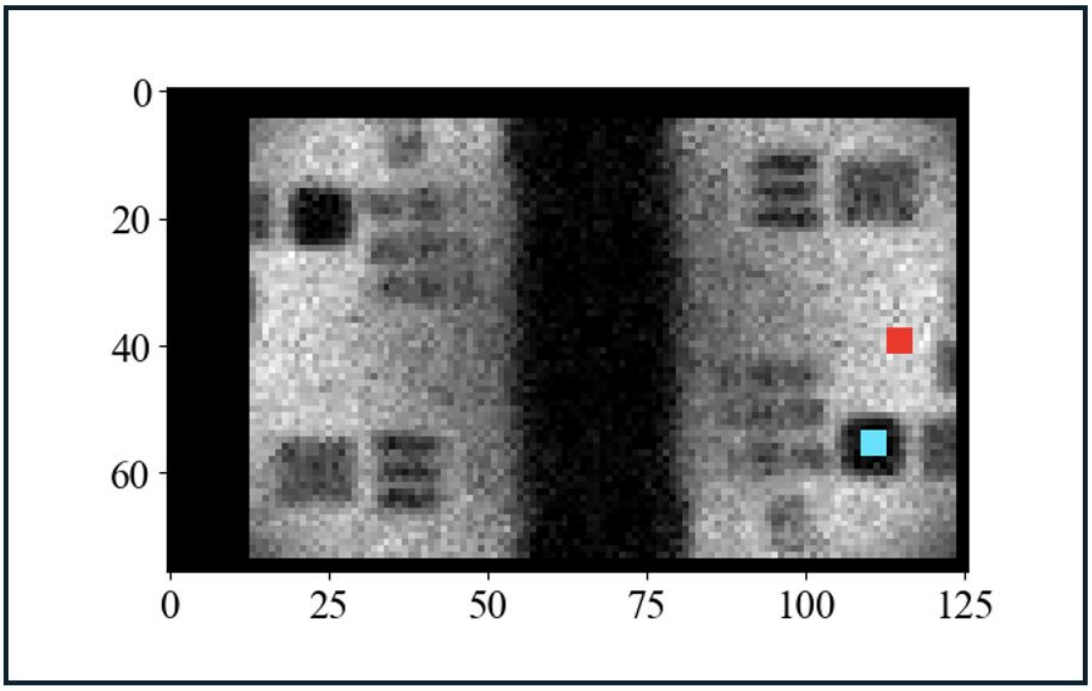


Figure S4. Varying integration limits to improve the contrast-to-noise ratio**.** We indicate the regions where the contrast-to-noise ratio was measured by the red and blue regions. The average intensity of the pixels in the red square is used to generate $\overline{I_1}$ and σ_1; that of the blue square, to generate $\overline{I_2}$ and σ_2.

Convergence in the Measured Error of the Quantum and the Classical Measurements.

To determine the selection of number of frames, *F,* and the number of measurements, *N*, acceptable for the error analysis, we performed the fitting procedure for a range of *N* and *F*, using classical image data, to verify that both are sufficiently high. As defined in the main text, *F* is the number of frames used to generate each image. In this discussion, one "measurement" the determination of the size of an object from its image (the result of the fitting procedure), where each image is obtained from the accumulation of *F* unique frames. For each slit size, one measurement is performed on each image. The convergence for the number of photons, *M*, comprising each image was computed indirectly, by computing the convergence based on the number of frames *F*, as $F \propto M$. (The exact proportionality factor between *F* and *M*, and thus the number of photons

Downloaded from pubs.acs.org/jpcbfk/article-supplement/5443067/pdf/jp6c03297_si_001/ by guest on 01 October 2026

199 comprising each image, can be established using the results from calibration, but is not strictly
200 necessary.) Using the same procedure used for determining the error in the fitted size, we varied
201 F while maintaining a sufficiently high N, and considered the standard deviation (error) of the N
202 measurements. As F increases, the error approaches an asymptote, and adding more frames does
203 not improve the image quality. Selecting a value near the asymptote (*e.g.* $F = 16{,}000$), we vary N.
204 We observe that as N is increased, the curve of standard deviation in the measured size versus size
205 becomes monotonic, then quite smooth. Adding additional measurements does not change the
206 standard deviation. Selecting an N where the standard deviation increases monotonically as the slit
207 size decreases is needed to establish that the standard deviation is genuine, rather than due to too
208 few frames.
209

Downloaded from pubs.acs.org/jpcbfk/article-supplement/5443067/pdf/jp6c03297_si_001/ by guest on 01 October 2026

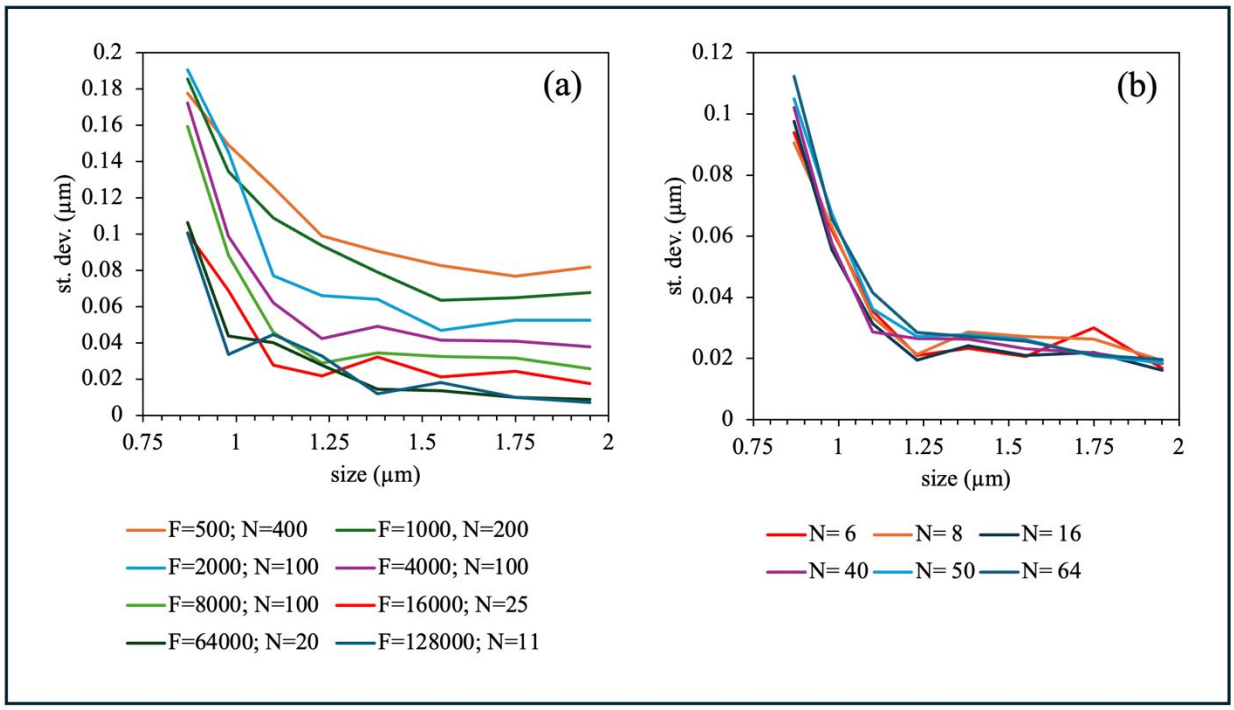


Figure S5. Convergence in the error in the measurement of bar sizes with respect to parameters affecting the number of photons used. F is the number of frames comprising one image. N is the number of measurements. Eq 6 of the main text, F, and the efficiency of the detector, η, are required to determine the number of photons in a given classical or quantum experiment.

(a) There is convergence in the errors for F = 16,000 frames and N = 21 measurements.

(b) The number of frames is held at F = 16,000. The variation in the standard deviation with bar size becomes monotonic between N = 16 and N = 40, indicating an acceptable minimum number of measurements.

Downloaded from pubs.acs.org/jpcbfk/article-supplement/5443067/pdf/jp6c03297_si_001/ by guest on 01 October 2026

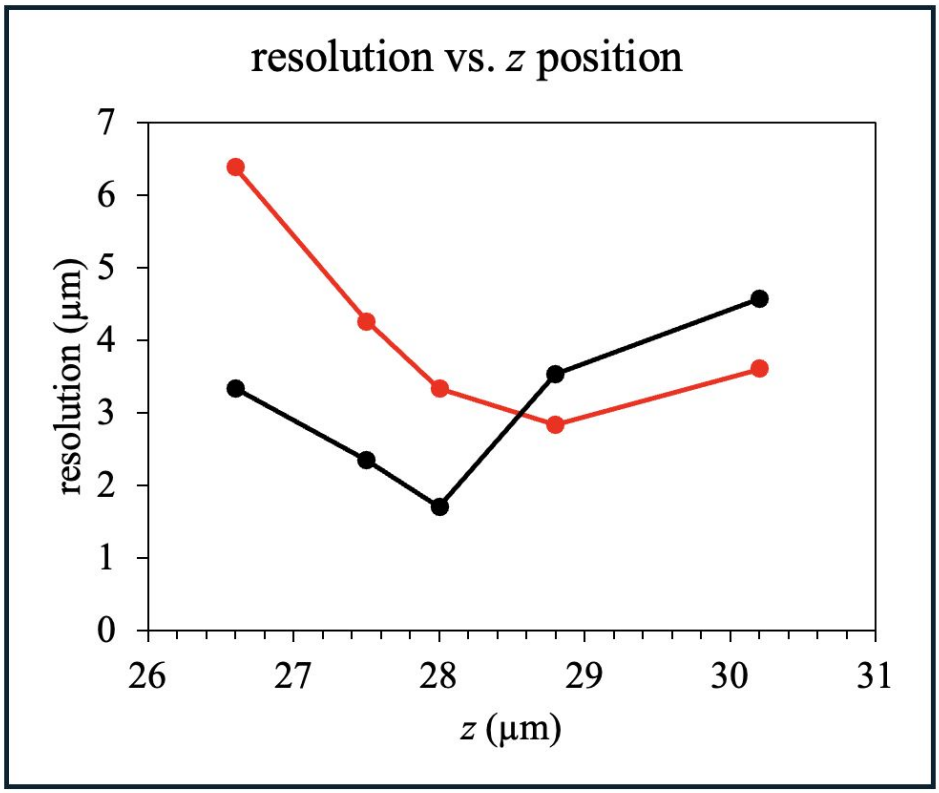


Figure S6. Optimization of the focus and the Heisenberg limit. The object is translated along the z axis (along the optical axis), and after obtaining a 1.5-million-frame data set, the resolution is measured for the classical (red) and quantum (black) image, from the data set obtained from five positions along the edge. The resolution is computed in the same manner as described in Methods. The position at z = 28.0 μm (relative to an arbitrary reference point), with a resolution ratio of 2.0 $\pm$ 0.2, was selected for error analysis, as it corresponds to the Heisenberg limit. Notably, the z position with the best resolution for the classical image is not the same position where the quantum image has the best resolution, or where the classical-to-quantum resolution ratio is the greatest. This result is qualitatively similar to that of He *et al.*[4]

The Cramér-Rao Lower Bound

The divergence of the error of the classical and quantum experiments presented in **Figure 6** were predicted by computing the Fisher information (FI) for the parameter we are estimating in this experiment: the size of the bar on each triple-bar object (s) (**Figure S7**, below). The Fisher information is defined as:

$$\mathrm{FI}(s) = \int p(x,\mathrm{NA},\lambda,\mu,s)\left(\frac{\partial \ln p(x,\mathrm{NA},\lambda,\mu,s)}{\partial s}\right)^2 dx\,. \qquad (12)$$

Downloaded from pubs.acs.org/jpcbfk/article-supplement/5443067/pdf/jp6c03297_si_001/ by guest on 01 October 2026

The FI is a function of the image, $p(x,\mathrm{NA},\lambda,\mu,s)$, to which the data are fit. The Cramér-Rao lower bound, CRLB is the inverse of the Fisher Information (FI). *It represents the lower bound of the error in an unbiased estimator*, in our case, the size of the bar being measured (s)[5].

$$\mathrm{CRLB} = \sigma(s)^2 \geq \frac{1}{\mathrm{FI}(s)}\,. \tag{13}$$

For each bar size (s) measured in **Figure 6**, we numerically compute the FI as a function of the bar size (s), holding the other parameters constant. For comparison, we take the classical image to be that obtained from 810-nm SPDC photons *with no effort to isolate entangled pairs*. For the quantum image, we approximate the CRLB as the classical CRLB of photons at the Heisenberg limit wavelength, 405-nm[5]. For an equivalent comparison between the experimentally measured relative error, we take the square root of the CRLB and divide by the known value for s to yield a relative CRLB error, a dimensionless quantity. The CRLB calculation (**Figure S7**) suggests that we may experimentally expect that imaging with 405-nm classical light (or 810-nm entangled photon pairs) will result in a measured relative error of about one-half that afforded by 810-nm photons under otherwise equivalent conditions. This is confirmed experimentally by the error in **Figure 6**, where the relative error in the bar measured from the quantum image is lower for all bar sizes compared to the classical image of the same s.

The magnitude of the relative error between the experimentally-obtained classical and the quantum measurements (**Figure 6**) is smaller than that observed between the CRLBs for 810-nm photons and for 405-nm photons, surrogates for entangled 810-nm photons (**Figure S7**). As noted in the Introduction, the computation of the CRLB was to motivate the experiments that produced **Figure 6**. It was never our goal to demonstrate quantitative superposition of the computed and experimental plots of standard deviation *vs*. slit separation. Consequently, we have relegated the CRLB plots to the SI as **Figure S7** and provided more context. It is important to keep in mind that

Downloaded from pubs.acs.org/jpcbfk/article-supplement/5443067/pdf/jp6c03297_si_001/ by guest on 01 October 2026

the CRLB curves in **Figure S7** are computed as a *single-parameter estimation*, likely an oversimplification. They also assume *a single measurement*. If multiple identical measurements are performed for the estimation of the error bars, as done for the construction of **Figure 6**, a noise model must be used for the theoretical estimation of multiple measurements CRLB. Indeed, this is what we did in Santra *et al*.[6] For N identical measurements the error bar will scale as $1/N^{1/2}$. For $N = 21$ in **Figure 6**, it is anticipated that the theoretical CRLB and the experimental error bar be roughly the same. The discrepancy might also partially be attributed to our model for the CRLB calculation not considering nuisance parameters, such as a shifting image centroid.

The discussion above is important and requires further comment. At issue here are the definition of the CRLB and the role of N. With regard to the CRLB, it must be appreciated that *the CRLB is defined for one measurement*, which, in turn requires the definition of one measurement—as we note above. With regard to N, for our case with N = 21, the CRLB does match the experimental data rather well when scaled by $(1/21)^{1/2}$. We have, however, intentionally avoided constructing a plot of the scaled CRLB against the experiments because we do not want to leave the reader with the impression that one can blithely scale by $(1/N)^{1/2}$ without using an appropriate noise model, as we did elsewhere.[6] Furthermore, scaling by $(1/N)^{1/2}$ must not be interpreted as implying that if $N \rightarrow \infty$, CRLB $\rightarrow 0$. The issue of the noise model notwithstanding, it may be impossible or impractical to characterize realistically the target one is imaging. This is the case in fluorescence-based, single-molecule measurements where bleaching and sample degradation limit N. More importantly, there is no way to make N go to infinity!

Downloaded from pubs.acs.org/jpcbfk/article-supplement/5443067/pdf/jp6c03297_si_001/ by guest on 01 October 2026

We posit that qualitative resemblance between the classical and quantum measurements and the 810-nm and 405-nm CRLB error curves affords theoretical support for our experimental observation (**Figures 4** and especially **6**) that quantum imaging reduces the error in measuring a parameter for a non-point-source object by a factor of approximately two. Hence, the CRLB calculation supports the observation in **Figure 6** that *quantum imaging slows the divergence in the measured error as the size of the object decreases*.[7]

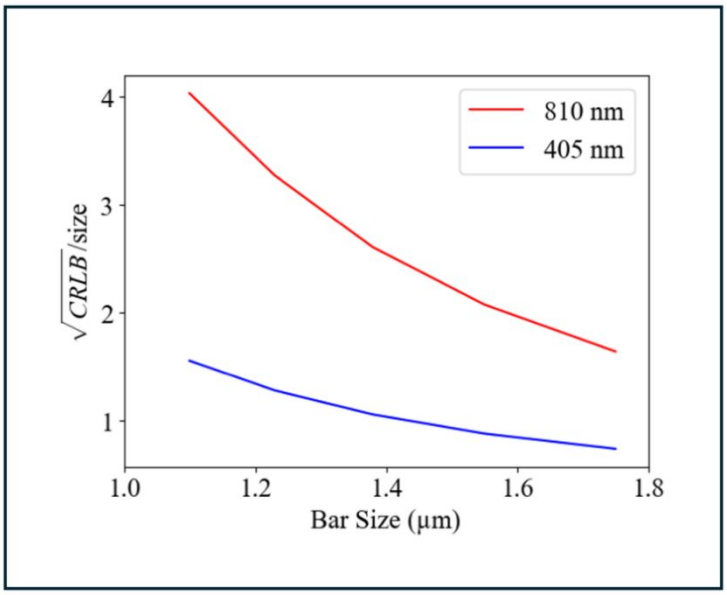


Figure S7. CRLB calculation for a triple-bar object imaged with a single lens. The CRLB is computed for our image function $p(x,\mathrm{NA},\lambda,\mu,s)$ along one dimension for the same bar sizes on the 1951 USAF resolution test chart whose errors are presented in **Figure 6**. $\sqrt{CRLB}/s$, the expected relative error as determined by the Fisher information, is plotted against bar size, s. The relative error expected when imaging with 405-nm light is approximately half the relative error expected when 810-nm light is used. The NA is obtained from the data used for the size fitting result shown in **Figure 6** (NA = 0.183).

Downloaded from pubs.acs.org/jpcbfk/article-supplement/5443067/pdf/jp6c03297_si_001/ by guest on 01 October 2026

References for Supporting Information

(1) Meda, A.; Ruo-Berchera, I.; Degiovanni, I. P.; Brida, G.; Rastello, M. L.; Genovese, M. Absolute Calibration of a Charge-Coupled Device Camera with Twin Beams. *Applied Physics Letters* **2014**, *105* (10), 101113. https://doi.org/10.1063/1.4895665.

(2) Avella, A.; Ruo-Berchera, I.; Degiovanni, I. P.; Brida, G.; Genovese, M. Absolute Calibration of an EMCCD Camera by Quantum Correlation, Linking Photon Counting to the Analog Regime. *Opt. Lett.* **2016**, *41* (8), 1841. https://doi.org/10.1364/OL.41.001841.

(3) Klyshko, D. N. Use of Two-Photon Light for Absolute Calibration of Photoelectric Detectors. *Sov. J. Quantum Electron.* **1980**, *10* (9), 1112–1117. https://doi.org/10.1070/QE1980v010n09ABEH010660.

(4) He, Z.; Zhang, Y.; Tong, X.; Li, L.; Wang, L. V. Quantum Microscopy of Cells at the Heisenberg Limit. *Nat Commun* **2023**, *14* (1), 2441. https://doi.org/10.1038/s41467-023-38191-4.

(5) Unternährer, M.; Bessire, B.; Gasparini, L.; Perenzoni, M.; Stefanov, A. Super-Resolution Quantum Imaging at the Heisenberg Limit. *Optica* **2018**, *5* (9), 1150. https://doi.org/10.1364/OPTICA.5.001150.

(6) Santra, K.; Nguyen, V.; Smith, E. A.; Petrich, J. W.; Song, X. Localization of Nonblinking Point Sources Using Higher-Order-Mode Detection and Optical Heterodyning: Developing a Strategy for Extending the Scope of Molecular, Super-Resolution Imaging. *J. Phys. Chem. B* **2021**, *125* (12), 3092–3104. https://doi.org/10.1021/acs.jpcb.0c10875.

(7) Tsang, M.; Nair, R.; Lu, X.-M. Quantum Theory of Superresolution for Two Incoherent Optical Point Sources. *Phys. Rev. X* **2016**, *6* (3), 031033. https://doi.org/10.1103/PhysRevX.6.031033.

Downloaded from pubs.acs.org/jpcbfk/article-supplement/5443067/pdf/jp6c03297_si_001/ by guest on 01 October 2026